npj | quantum materials

Article

Published in partnership with Nanjing University

https://doi.org/10.1038/s41535-024-00655-1

Electrical detection of mobile skyrmions with 100% tunneling magnetoresistance in a racetrack-like device

Mengqi Zhao[1,2,12], Aitian Chen[3,12], Pei-Yuan Huang[4,5,12], Chen Liu[3,12], Laichuan Shen[6,12], Jiahao Liu[7,8] ✉, Le Zhao[1,2], Bin Fang[3], Wen-Cheng Yue[4,5], Dongxing Zheng[3], Ledong Wang[1,2], Hao Bai[1,2], Ka Shen[6], Yan Zhou[9], Shasha Wang[10], Enlong Liu[10], Shikun He[10], Yong-Lei Wang[4,5] ✉, Xixiang Zhang[3] ✉ & Wanjun Jiang[1,2,11] ✉

Magnetic skyrmions are topological spin textures that are regarded as promising information carriers for next-generation spintronic memory and computing devices. For practical applications, their deterministic generation, manipulation, and efficient detection are the most critical aspects. Although the generation and manipulation of skyrmions have been extensively studied, efficient electrical detection of mobile skyrmions by using techniques that are compatible with modern magnetic memory technology, remains to be adequately addressed. Here, through integrating magnetic multilayers that host nanoscale skyrmions, together with the magnetic tunnel junctions (MTJ), we demonstrate the electrical detection of skyrmions by using the tunneling magnetoresistance (TMR) effect with a TMR ratio that reaches over 100% at room temperature. By building prototype three-terminal racetrack-like devices, we further show the electrical detection of mobile skyrmions by recording the time-dependent TMR ratios. Along with many recent developments, our results could advance the development of skyrmionic memory and logic devices.

Magnetic skyrmions, a type of topological spin textures[1–13], have drawn growing attention due to their potential applications[8,9,12,14], such as racetrack memory[14–16], logic gates[17,18], and quantum qubits[19–21]. These particle-like spin configurations can be stabilized in a range of symmetry-breaking magnets[1,2,22–26]. However, compared with skyrmions in various bulk materials[2,3,27], skyrmions in asymmetric magnetic multilayers are of particular interest for potential device applications[8,9,12,22–24]. For example, nanoscale Néel skyrmions can be stabilized at room temperature in these multilayers, and their manipulation can be achieved through current-induced spin-orbit torques (SOT)[22–24]. These ingredients are key for numerous skyrmionic applications. More importantly, these multilayers can be integrated with magnetic tunnel junction (MTJ) that subsequently enables an efficient readout of nanoscale skyrmions[28]. Despite significant progress made on the generation and manipulation of skyrmions[22–24,29–32], it remains challenging to obtain efficiently electrical readout of skyrmions[33,34], which is a major bottleneck for skyrmionic applications.

MTJ is the fundamental building block of magnetoresistive random access memory (MRAM) technology[35–37]. It is made of a sandwich-like trilayer that contains two metallic magnetic layers separated by a thin insulating tunneling barrier (typically MgO). Governed by the quantum-mechanical tunneling effect, electrons can transport from one metallic magnetic layer, through the insulator barrier, to the other metallic magnetic

[1]State Key Laboratory of Low-Dimensional Quantum Physics and Department of Physics, Tsinghua University, 100084 Beijing, China. [2]Frontier Science Center for Quantum Information, Tsinghua University, 100084 Beijing, China. [3]Physical Science and Engineering Division, King Abdullah University of Science and Technology, Thuwal 23955–6900, Saudi Arabia. [4]Research Institute of Superconductor Electronics, School of Electronic Science and Engineering, Nanjing University, Nanjing 210023, China. [5]National Key Laboratory of Spintronics, Nanjing University, Suzhou 215163, China. [6]The Center for Advanced Quantum Studies and Department of Physics, Beijing Normal University, 100875 Beijing, China. [7]College of Advanced Interdisciplinary Studies & Hunan Provincial Key Laboratory of Novel Nano-Optoelectronic Information Materials and Devices, National University of Defense Technology, Changsha 410073 Hunan, China. [8]Nanhu Laser Laboratory, National University of Defense Technology, Changsha 410073, China. [9]School of Science and Engineering, The Chinese University of Hong Kong, Shenzhen 518172 Guangdong, China. [10]Zhejiang Hikstor Technology Co. LTD., 1718, Chongwen Road, Hangzhou, China. [11]Collaborative Innovation Center of Quantum Matter, 100084 Beijing, China. [12]These authors contributed equally: Mengqi Zhao, Aitian Chen, Pei-Yuan Huang, Chen Liu, Laichuan Shen.
✉e-mail: liujiahao20@nudt.edu.cn; yongleiwang@nju.edu.cn; xixiang.zhang@kaust.edu.sa; jiang_lab@tsinghua.edu.cn

layer. Because of the spin-dependent density of states near the Fermi energy in the magnetic layers, the tunneling electrons are spin-polarized. Consequently, the parallel and antiparallel magnetization orientations of these two magnetic layers give rise to the low and high TMR levels[35–37]. Since the TMR effect can convert the presence and absence of magnetic textures into strong electrical signals with large on/off ratios, it is thus expected to be advantageous for the efficient electrical detection of skyrmions[28]. A few recent efforts have been made to implement the TMR effect for skyrmion detection in magnetic multilayers[38–44], which, however, are either limited by a relatively low TMR ratio[41,42], or by immobile skyrmions[39,42–44] that hinder the subsequent spin torque manipulation. These two aspects limit the application of skyrmions in situations where mobile skyrmions are prerequisites (racetrack memory[14], reservoir computing[12,45], etc.), which motivate the present study.

Here, we study the feasibility of integrating representative $[Pt/Co/Ta]_{10}$ multilayers that host nanoscale skyrmions[23,46] with MTJ of stacking order CoFeB/MgO/CoFeB[42,47]. Through optimizing the skyrmionic MTJ stack, we demonstrate the electrical detection of skyrmions with a 100% TMR ratio at room temperature. Further, we show that the transportation of skyrmions in the racetrack can be readout by using a nanoscale MTJ pillar with the change of TMR over 1.3 kΩ.

Results

Optimization of skyrmionic MTJ

The concept of skyrmion racetrack device is schematically shown in Fig. 1a, which consists of mobile skyrmions and the TMR detection[14,48]. In this type of devices, skyrmions can move along a nanowire made of magnetic multilayers, which is driven by the current-induced spin torque[22,23,31]. Underneath the MTJ pillar, the presence and absence of skyrmions, which is reflected as the change of magnetization in the free layer, can be electrically detected via outputting the low and high TMR levels[28].

To experimentally demonstrate the stabilization, manipulation, together with the TMR detection of mobile skyrmions, we deposit multilayers of stacking order: Ta(5)/$[Pt(2.5)/Co(1)/Ta(0.5)]_{10}$/Ta(0.5)/CoFeB(0.9)/MgO(1.7)/CoFeB(1.1)/Ta(0.5)/Co(0.3)/$[Pt(1.5)/Co(0.4)]_2$/Ru(0.85)/$[Co(0.5)/Pt(1.5)]_3$/Ru(5) (thickness in nm), as schematically illustrated in Fig. 1b. In these multilayers, the bottom interfacially asymmetric multilayer $[Pt(2.5)/Co(1)/Ta(0.5)]_{10}$ could host room-temperature Néel-type skyrmions[23,46]. Through optimizing the thickness of the inserted Ta layer (0.5 nm) and the bottom $CoFeB_1$ free layer (0.9 nm), the $[Pt/Co/Ta]_{10}$ multilayer could be ferromagnetically coupled to the bottom $CoFeB_1$ free layer (Supplementary Note 1). This suggests that the noncollinear spin textures, including chiral domain walls and magnetic skyrmions in the $[Pt/Co/Ta]_{10}$ multilayer can be imprinted onto the bottom $CoFeB_1$ free layer. Namely, the bottom $CoFeB_1$ and $[Pt/Co/Ta]_{10}$ synergistically act as a hybrid free layer. The top $CoFeB_2$ reference layer (1.1 nm) is pinned by a synthetic antiferromagnet (SAF) made of Co(0.3)/$[Pt(1.5)/Co(0.4)]_2$/Ru(0.85)/$[Co(0.5)/Pt(1.5)]_3$. In particular, the choice of MTJ stack made of $CoFeB_1$(0.9)/MgO(1.7)/$CoFeB_2$(1.1) with perpendicular magnetic anisotropy (PMA) could be advantageous for maintaining a high TMR ratio[42,47], as compared with Co/MgO/Co system[41,49].

The layered growth of film stack is verified by conducting a high-angle annular dark-field scanning transmission electron microscopy (HAADF-STEM) experiment, as illustrated in the right panel of Fig. 1b. Here, one can clearly identify the layered structure of $[Pt/Co/Ta]_{10}$ multilayer, the $CoFeB_1$/MgO/$CoFeB_2$ trilayer, and the $[Pt/Co]_3$/Ru/$[Pt/Co]_3$ synthetic antiferromagnet (SyAF) layer. The out-of-plane magnetic hysteresis loop ($M-H_z$) is measured and shown in Fig. 1c. Distinct jumps reflect the switching of each magnetic layers, which are marked by arrows of different colors, respectively. The shadowed area in Fig.1c corresponds to the magnetic signal of the $[Pt/Co/Ta]_{10}$ multilayer, the shape of which is consistent with those multilayers that host Néel-type skyrmions[23,24,30,33,46].

Identification of skyrmion phase in the [Pt/Co/Ta]10 multilayer

Shown in Fig. 2a are the $M-H_z$ loops of the $[Pt/Co/Ta]_{10}$ multilayer that are measured under different temperatures. Shapes of these loops are similar to those typical asymmetric multilayers that host room temperature skyrmions, such as $[Pt/Co/Ta]_n$[23,46], $[Pt/Co/Ir]_n$[8,30,33], and $[Pt/Co/Fe/Ir]_n$[24], implying a possible existence of Néel-type magnetic textures in the present material system. Following the decreased temperature, shapes of $M-H_z$ loops change slightly. This reflects a temperature dependent magnetic property, which can be further inferred from the extracted saturation magnetization (M_s), as shown in the inset to Fig. 2a. Such a temperature dependent magnetism suggests that the resultant skyrmionic phase could be temperature sensitive. Moreover, shapes of $M-H_z$ loop obtained from the $[Pt/Co/Ta]_{10}$ multilayer and from the corresponding multilayers contained in MTJ stack are consistent, as marked by the shaded area in Fig. 1c (Supplementary Note 2). This suggests a limited influence to the skyrmionic multilayer by the subsequent growth of the MTJ stack[50].

To directly verify the existence of Néel skyrmions in the $[Pt/Co/Ta]_{10}$ multilayer, Lorentz transmission electron microscopy (LTEM) experiment is conducted. As shown in Fig. 2b, bright and dark contrasts corresponding to skyrmions can be observed, which are done with a tilting angle 30°, defocus length −3 mm and the magnetic field 360 Oe. We also perform LTEM at a different defocus length at 0 mm, and find that the contrast disappears at 0 mm, which is the characteristic feature of Néel skyrmions[51,52]. Detailed description can be found in Supplementary Note 3.

The manipulation of skyrmions by the current-induced spin torque, is demonstrated in the nanostructured device made of $[Pt/Co/Ta]_{10}$ multilayer (shown in Fig. 2c) by conducting a magnetic force microscopy (MFM) experiment. In a 1-μm-wide nanowire, the coexistence of skyrmions and stripe domains at zero field can be found, as shown in Fig. 2d. After applying a pulse current of amplitude $J = 1.0 \times 10^7$ A/cm^2 and of duration 10 ns, a morphological transformation from stripe domain into isolated skyrmions is observed, together with a migration of skyrmions along the nanowire, as shown in Fig. 2e. More experimental data and analyses can be found in Supplementary Note 4. This experiment reveals the feasibility of electrical manipulation of nanoscale skyrmions by using the current-induced spin torques, a method that has been frequently discussed in similar multilayers[22,23,31,48,53].

Characterization of nanoscale skyrmionic MTJs

Based on the optimized film stack, we subsequently fabricate nanoscale skyrmionic MTJ devices, as shown in Fig. 3a. We use an argon ion milling system that is equipped with an end-point detector, which ensures a successful fabrication of skyrmionic MTJ, while maintaining the magnetic properties of the $[Pt/Co/Ta]_{10}$ multilayer to be unattacked, as schematically shown in Fig. 1a. The width of the racetrack is 1 μm, and the diameter of the MTJ pillar is 500 nm, respectively. Four-terminal electrical resistance measurements are conducted by employing standard AC lock-in technique, with applied currents of 200 nA and a frequency of 17 Hz across the MTJ device (in the current-perpendicular-plane geometry). Figure 3b demonstrates the corresponding TMR data that is measured as a function of H_z. By scanning the H_z from positive to negative (blue curve), the TMR curve exhibits a clear step due to the antiferromagnetic coupling of the SAF pinning layers around 1.4 kOe. By gradually decreasing field, the bottom $CoFeB_1$ free layer switches together with the $[Pt/Co/Ta]_{10}$ multilayer at field between ± 0.6kOe, as a result of ferromagnetic coupling between them. The corresponding TMR ratio can be calculated as

$$\mathrm{TMR}(\%) = \frac{[R_{AP} - R_P]}{R_P} \times 100\% \quad (1)$$

where $R_{AP} = 22.44\,\mathrm{k\Omega}$, and $R_P = 11.03\,\mathrm{k\Omega}$ are the high and low TMR states, which correspond to the complete antiparallel and parallel alignments of the free layer and the reference layer, respectively. In particular, we find that the TMR ratio could reach up to 103.45% at room temperature.

The free layer of the skyrmionic MTJ device, composed of the bottom $CoFeB_1$ (0.9 nm) and the ferromagnetically coupled $[Pt/Co/Ta]_{10}$ multilayer, exhibits a small switching field as compared with the top $CoFeB_2$ (1.1 nm) reference layers. Subsequently, we focus on the minor loop measurements,

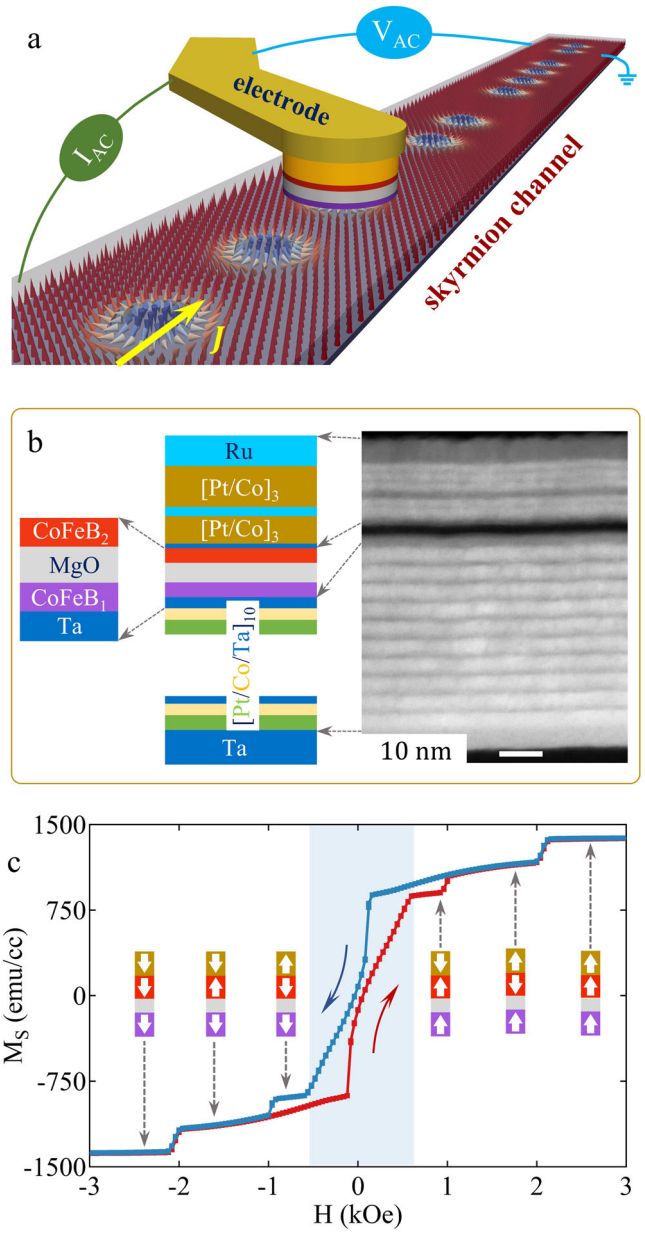

Fig. 1 | Illustration and experimental realization of skyrmionic MTJ. a Schematic of skyrmion racetrack and its electrical detection setup via using an MTJ. **b** Skyrmion MTJ stack (left) and HAADF-STEM image (right) of the cross-sectional MTJ films. The hybrid free layer consists of the skyrmion hosting multilayer $[Pt/Co/Ta]_{10}$ and the bottom $CoFeB_1$ free layer, which are ferromagnetically coupled through an ultrathin Ta layer (Ta layer in left inset, 1 nm in total). Left inset: MTJ with the top reference layer ($CoFeB_2$) and the bottom free layer ($CoFeB_1$) sandwiched by the MgO layer. **c** Magnetic hysteresis loop of the skyrmionic MTJ stack. The inset shows the magnetic configurations of different layers. The purple, red, and brown arrows refer to the magnetization orientations of the hybrid free layer ($[Pt/Co/Ta]_{10}$ and $CoFeB_1$), the $CoFeB_2$ reference layer, and the top part of the SAF, respectively.

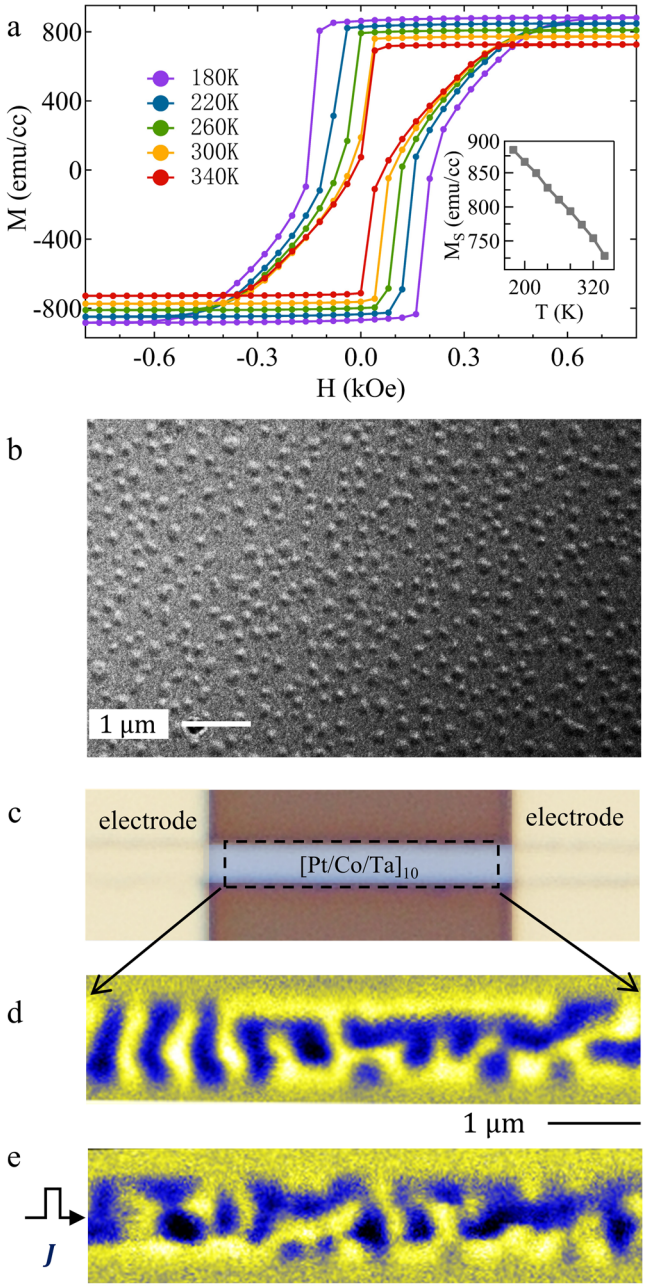

Fig. 2 | Skyrmions in the $[Pt/Co/Ta]_{10}$ multilayer. a Out-of-plane magnetic hysteresis loops of the skyrmion hosting multilayer $[Pt/Co/Ta]_{10}$ at various temperatures. Inset: the evolution of saturation magnetization as a function of temperature. **b** A direct identification of skyrmion by using Lorentz electron transmission microscopy (LTEM). **c** Optical micrograph of a 1 μm-wide skyrmion channel. **d**, **e** The magnetic force microscopy (MFM) images that were taken before and after applying a current pulse ($J = 1.0 \times 10^7$ A/cm^2, 10 ns), all at zero field.

which reveal information on the magnetization dynamics of the free layer in the region that is underneath the MTJ pillar. Through fixing the magnetization of the top $CoFeB_2$ (1.1 nm) reference layer being downward (upward), minor loop measurements reveal intermediate and discretized TMR states, as shown in Fig. 3c, d, respectively. These discretized TMR steps suggest the existence of multidomain states in the free layer, which change their configurations during the minor loop measurement. As a result, evolving domain configurations underneath the MTJ pillar produce discretized TMR steps. Similar minor loop measurements were repeated for several times in the same device, in which similar TMR loops with discretized steps of different heights and nucleation fields can be observed. This observation could be attributed to the randomly distributed disorders in the free layer, which result in a random distribution of magnetic domains and skyrmions in the region that is underneath the MTJ pillar. Moreover, a consistent yield of TMR ratio over 100% can be found in 42 devices which were made on the same batch (raw data of which can be found in Supplementary Note 5).

TMR measurements at different temperatures

We further investigate the performance of skyrmionic MTJ at different temperatures. This is motivated by the fact that $[Pt/Co/Ta]_{10}$ multialyer

exhibits a temperature sensitive magnetization (as shown in Fig. 2a). Figure 4a shows appreciable TMR ratio and clear switching processes in the temperature range from 180 K to 340 K. The TMR ratio increases with the decreased temperature, and reaches 133.3% at 180 K. Temperature-dependent antiparallel (R_{AP}) and parallel (R_P) TMR values can be found in Supplementary Note 6. The increase of TMR ratio mainly results from the increase of R_{AP}, whereas R_P remains nearly the same with the decreased tempareture[36]. The corresponding minor loops are also measured, as shown in Fig. 4b. Following the decrease of temperature, shapes of minor loops evolve accordingly, which are consistent with the change of magnetic properties as a function of temperature. When the temperature is lower than 220 K, only one sharp switching event can be observed, indicating the occurrence of uniform magnetization switching of the free layer in the region underneath the MTJ pillar. In the temperature range between 260 K and 340 K, discretized TMR steps can be found. In particular, increased temperatures lead to the formation of labyrinthine domains and skyrmions in the free layer, which shrink in size and result in the reduced TMR steps in the minor loop measurement.

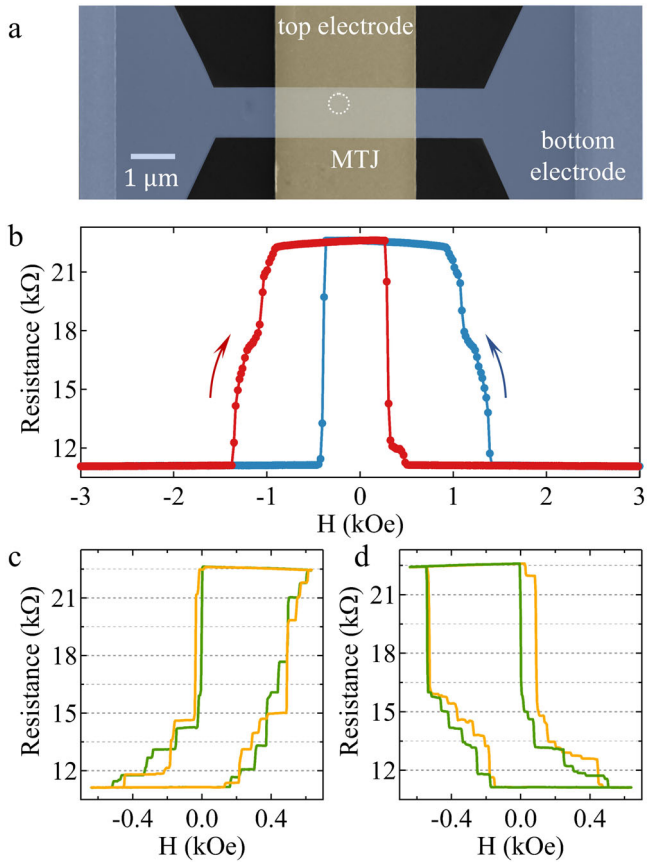

Fig. 3 | TMR performances of nanoscale skyrmionic MTJ. a An SEM image of the nanoscale skyrmionic MTJ device. **b** Room-temperature TMR curves that are measured as a function of the out-of-plane magnetic field. **c**, **d** Two independent minor loops of the TMR measurement, with the magnetization orientation of the top $CoFeB_2$ reference layer pointing downward and upward, respectively.

TMR readout of mobile skyrmions

To demonstrate the skyrmionic racetrack performance, one needs to electrically read out mobile skyrmions by using TMR[14]. This could be done in our nanodevices by passing pulse currents along the nanowire in the current-in-plane geometry, implementing the spin Hall effect and the resultant spin torques in the Pt underlayer[8,11,23,48,53]. As a result, the transportation of skyrmonic spin textures along the racetrack that is made of $[Pt(2.5)/Co(1)/Ta(0.5)]_{10}/Ta(0.5)/CoFeB(0.9)$ free layer can be triggered by passing pulse currents (J). The subsequent electrical readout of skyrmions by using the MTJ is done by passing a small AC probing current (200 nA, 17 Hz) across the TMR device (in the current-perpendicular-plane geometry). At zero field, when repetitively applying 5 current pulses of amplitude $J = 1.96 \times 10^7 A/cm^2$, a duration of 500 ns, and an interval of 1 ms along the racetrack, the time-dependent TMR signals are recorded, as shown in the bottom panel of Fig. 5a. The evolution of TMR signals exhibits clear responses after applying each current burst (J), suggesting the change of domain configurations in the free layer, likely the skyrmion displacement and transformation that are induced by the spin torques.

To qualitatively understand the origin of time-dependent TMR signals that are induced by applying current pulses along the racetrack, we perform micromagnetic simulations to characterize the change of magnetization configurations. Detailed description, together with material specific parameters of micromagnetic simulations can be found in methods and Supplementary Note 7. Figure 5b shows the simulated skyrmion transportation along the racetrack that is driven by the current-induced spin torques. Upon applying different numbers of pulse currents ($J = 8.3 \times 10^7 A/cm^2$, 5 ns), one clearly identifies the displacement of stripe domains and isolated skyrmions. Underneath the MTJ pillar (marked by the yellow circle in Fig. 5b), the amplitude of out-of-plane net magnetization (m_z) of the free layer and its time-dependent change are extracted and shown in Fig. 5c by the blue circle. By utilizing a parallel resistor model, and based on the measured low ($R_P = 11.03\,k\Omega$) and high ($R_{AP} = 22.44\,k\Omega$) TMR values, the TMR values

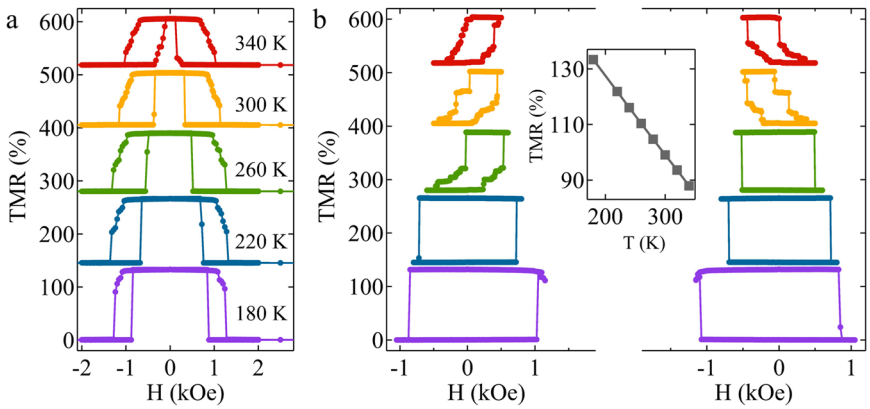

Fig. 4 | TMR measurements under different temperatures. a TMR loops of skyrmionic MTJ at various temperatures. **b** Minor TMR loops at various temperatures with the magnetization orientation of the top reference layer ($CoFeB_2$) pointing downward (left) and upward (right). The changed shapes of minor loops could be attributed to the variation of magnetic textures in the bottom skyrmion multilayer $[Pt/Co/Ta]_{10}$. Inset is the extracted temperature-dependent TMR ratio. The TMR loops are vertically shifted for clarity.

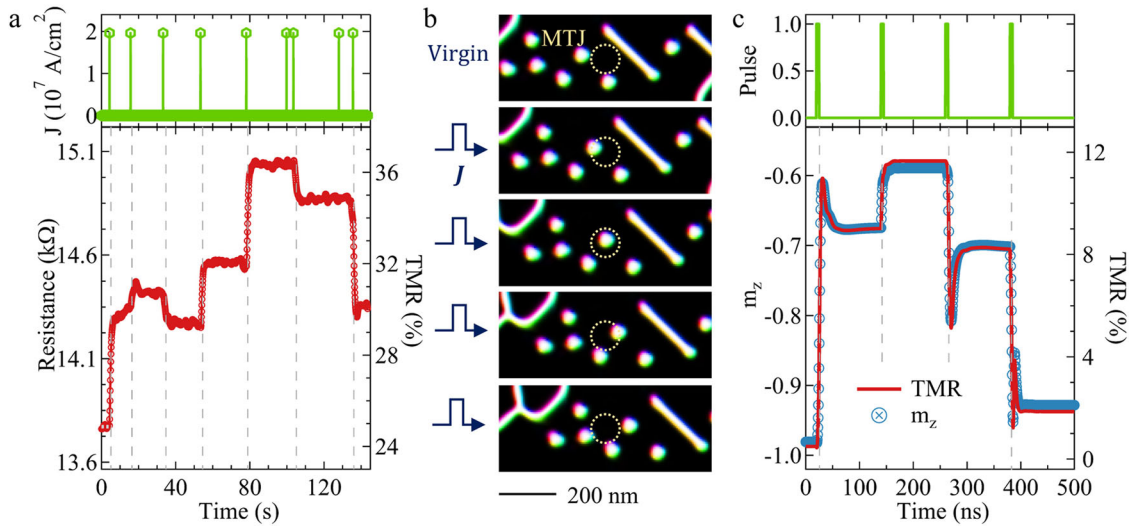

Fig. 5 | Electrical detection of current-driven skyrmion. a The time-dependent TMR that is obtained after applying current pulses along the bottom racetrack, with an amplitude $J = 1.96 \times 10^7$ A/cm^2 (upper panel). The change of TMR ratio with current pulses, indicating the change of domain configurations in the bottom channel (lower panel). **b** Simulated motion of skyrmions and stripe domains after applying each current pulse. **c** Simulated evolution of out-of-plane magnetization, m_z, under the MTJ pillar (blue marker) and the corresponding TMR ratio that is estimated based on experiment parameters (red line).

arising from skyrmions at different fields [$R(H)$] can be estimated as[54,55]

$$\frac{S_{MTJ}}{R(H)} = \frac{S_{AP}}{R_{AP}} + \frac{S_P}{R_P} \quad (2)$$

where S_{MTJ}, S_{AP}, and S_P represent the size of the MTJ pillar, the area with antiparallel/parallel magnetization configurations, respectively. Detailed caculation of $R(H)$ and TMR ratio ($\mathrm{TMR}(\%) = [R(H) - R_P]/R_P \times 100\%$) can be found in Supplementary Note 8. In particular, the corresponding TMR ratio can be estimated based on the amplitude of m_z of the free layer, as shown by the red line in Fig. 5c. The TMR ratio exhibits immediate responses after applying each pulse. This observation is consitent with our experimental results shown in Fig. 5a. When a part of the skyrmion moves underneath the MTJ pillar, the TMR ratio increases to an intermediate state. The signal reaches the highest level as the skyrmion is completely located underneath the MTJ pillar, which decreases when the skyrmion moves away from the MTJ pillar. Since the diameter of skyrmion size (approximately 400 nm in Fig. 2d) is smaller than the size of the MTJ pillar (500 nm), we cannot realize a completely antiparallel magnetization configuration in our experiment. This explains a reduced TMR ratio that is smaller than 100% in our simulation result.

The TMR detection of mobile skyrmions is also repetitively conducted for the same device under 0.35 kOe and in MTJs with different pillar sizes (Supplementary Note 9). There, one can consistently observe the emergence of discrete plateaus after applying current pulses along the bottom track. Through analyzing the resistance plateaus, we have identified that 19 kΩ is the most frequently occurring value. Through comparing with the calculated TMR results from micromagnetic simulations, such a value could be attributed to the electrical signature of a single skyrmion underneath the MTJ pillar. In addition, the plateau values for devices with pillar diameters of 500, 300 and 150 nm are in consistent with the prediction of Eq. (2).

Discussion

We have experimentally studied skyrmionic magnetic tunnel junctions (MTJs), which is done by integrating skyrmion-hosting multilayers [Pt/Co/Ta]$_{10}$ with CoFeB/MgO/CoFeB that exhibit a large tunneling magnetoresistance (TMR). Through optimizing the skyrmionic stack and MTJ fabrication process, we have successfully realized nanoscale skyrmionic MTJ with a 100% TMR ratio. In particular, the TMR signature of mobile skyrmions is revealed by applying pulse current along the skyrmion racetrack. It should be emphasized here that a simultaneous imaging of mobile skyrmions, and electrical readout by the TMR effect are remaining technical challenges. Meanwhile, miniaturized racetrack with width that is comparable with the diameter of skyrmions is also demanded in the future. Nevertheless, our work provides meaningful insights for implementing skyrmion-based devices that could promote the next-generation skyrmionic memory, logic and circuit.

Methods

Film growth

The MTJ stacks of composition and stacking order: Ta(5)/[Pt(2.5)/Co(1)/Ta(0.5)]$_{10}$/Ta(0.5)/$Co_{40}Fe_{40}B_{20}$(0.9)/MgO(1.7)/$Co_{40}Fe_{40}B_{20}$(1.1)/Ta(0.5)/Co(0.3)/[Pt(1.5)/Co(0.4)]$_2$/Ru(0.85)/[Co (0.5)/Pt(1.5)]$_3$/Ru(5) (thicknesses in nm) is deposited on the thermally oxidized Si substrates. This is done by using a Singulus ROTARIS magnetron sputtering system at room temperature with a base pressure of 1×10^{-6} Pa. A companion skyrmion hosting multilayer of stacking order Ta(5)/[Pt(2.5)/Co(1)/Ta(0.5)]$_9$/Pt(2.5)/Co(1)/Ta(2) is also deposited on the standard Si substrate for magnetometry measurement, and on the 30 nm thick Si_3N_4 membrane (CleanSiN) for Lorentz TEM experiment.

Magnetic characterization

Magnetic properties are studied by using a Quantum Design superconducting quantum interference device (SQUID) magnetometer. For the skyrmionic MTJ stack, the saturation magnetization is measured as M_s = 1380 emu/cc at room temperature. For the skyrmion-hosting multilayer, a saturation magnetization M_s = 774 emu/cc and an anisotropy field H_k = 11 kOe are determined. The magnetic domain structures are investigated using Titan Cs_Image TEM (FEI) in the Lorentz-Fresnel mode. The objective lens is turned off before the loading sample into the TEM instrument. The external magnetic field is controlled by slowly tuning the current of the objective lens. Due to the domain structures being Néel-type, the tilting angle is set at 30° and the defocused values are −3 and 0 mm. Magnetic force microscopy (MFM) imaging is conducted in a custom-designed MFM system, an atto-AFM/MFM from Attocube.

Device fabrication

The electron beam lithography is done by using the JEOL JBX-6300 FS lithography system, with a ma-N 2403 negative resist to pattern the bottom

electrode. We etch all the layers using Ar ion milling, which is followed by a removal of the resist using mr-Rem 500. Subsequently, MTJ pillars in circular shape with diameters ranging from 150 nm to 3 μm are defined using electron beam lithography with a ma-N 2403 negative resist. After etching the film below the MgO layer, a 30 nm thickness of SiO_2 is sputtered to ensure the electrical separation of the top the bottom contacts of the MTJs. A third electron beam lithography step with PMMA positive resist (Mirco-Chem, 950 PMMA A4) is then performed to pattern the electrode, followed by a subsequent deposition of Ti (10 nm)/Au (80 nm). Then a photolithography step with positive AZ5214 photoresist is performed to pattern the second electrode using an EVG 6200 mask aligner. Finally, the patterned MTJ devices are annealed in vacuum at 300 °C for 1 h with a perpendicular magnetic field of 8 kOe.

Electrical measurements

The TMR experiment is conducted by using the AC lock-in technique and the four-terminal method. An AC current of 200 nA and 17 Hz (Keithley 6221A current source) is applied across the MTJ device, and a lock-in amplifier (SR830) was used to measure the AC voltage. Temperature-dependent TMR is performed using a Quantum Design Physical Property Measurement System (PPMS). The response of the MTJ device to bias voltage can be found in Supplementary Note 10 and 11.

Micromagnetic simulations

The micromagnetic simulations are performed by using the Mumax3 software[56]. In the presence of spin torques, the underlying magnetization dynamics can be captured by performing the layer-resolved micromagnetic simulations, which is done by using Landau–Lifshitz–Gilbert (LLG) equation. We considered 10 dipole-coupled magnetic layers with thickness of 1 nm and spacing of 3 nm in the simulations, and used a discretization cell of $5 \times 5 \times 1\ \mathrm{nm}^3$. The parameters are: the exchange constant $A = 15\ \mathrm{pJ \cdot m^{-1}}$, the damping parameter $\alpha = 0.3$, the saturation magnetization $M_s = 800\ \mathrm{kA/m}$, the perpendicular magnetic anisotropy $K_u = 440\ \mathrm{kJ/m^3}$, the interfacial Dzyaloshinskii–Moriya exchange coefficient $D = 3\ \mathrm{mJ \cdot m^{-2}}$. The current pulses are of amplitude $8.3 \times 10^{11}\ \mathrm{A \cdot m^{-2}}$, duration 5 ns, and interval 115 ns.

Data availability

The data for the results presented in the paper and Supplementary Information are available from the corresponding author upon reasonable request.

Received: 29 December 2023; Accepted: 7 May 2024;
Published online: 14 June 2024

References

1. Rößler, U. K., Bogdanov, A. N. & Pfleiderer, C. Spontaneous skyrmion ground states in magnetic metals. *Nature* **442**, 797–801 (2006).
2. Mühlbauer, S. et al. Skyrmion Lattice in a Chiral Magnet. *Science* **323**, 915–919 (2009).
3. Yu, X. Z. et al. Real-space observation of a two-dimensional skyrmion crystal. *Nature* **465**, 901–904 (2010).
4. Nagaosa, N. & Tokura, Y. Topological properties and dynamics of magnetic skyrmions. *Nat. Nanotechnol.* **8**, 899–911 (2013).
5. Everschor-Sitte, K. & Sitte, M. Real-space Berry phases: Skyrmion soccer (invited). *J. Appl. Phys.* **115**, 172602 (2014).
6. Soumyanarayanan, A., Reyren, N., Fert, A. & Panagopoulos, C. Emergent phenomena induced by spin-orbit coupling at surfaces and interfaces. *Nature* **539**, 509–517 (2016).
7. Wiesendanger, R. Nanoscale magnetic skyrmions in metallic films and multilayers: a new twist for spintronics. *Nat. Rev. Mater.* **1**, 16044 (2016).
8. Jiang, W. J. et al. Skyrmions in magnetic multilayers. *Phys. Rep.* **704**, 1–49 (2017).
9. Fert, A., Reyren, N. & Cros, V. Magnetic skyrmions: advances in physics and potential applications. *Nat. Rev. Mater.* **2**, 17031 (2017).
10. Jiang, W. J. et al. Direct observation of the skyrmion Hall effect. *Nat. Phys.* **13**, 162–169 (2017).
11. Litzius, K. et al. Skyrmion Hall effect revealed by direct time-resolved X-ray microscopy. *Nat. Phys.* **13**, 170–175 (2017).
12. Everschor-Sitte, K., Masell, J., Reeve, R. M. & Kläui, M. Perspective: Magnetic skyrmions—Overview of recent progress in an active research field. *J. Appl. Phys.* **124**, 240901 (2018).
13. Wang, C.-J. et al. Formation of magnetic biskyrmions mediated by an intrinsic emergent monopole-antimonopole pair. *npj Quantum Mater.* **7**, 78 (2022).
14. Fert, A., Cros, V. & Sampaio, J. Skyrmions on the track. *Nat. Nanotechnol.* **8**, 152–156 (2013).
15. Sampaio, J., Cros, V., Rohart, S., Thiaville, A. & Fert, A. Nucleation, stability and current-induced motion of isolated magnetic skyrmions in nanostructures. *Nat. Nanotechnol.* **8**, 839–844 (2013).
16. Tomasello, R. et al. A strategy for the design of skyrmion racetrack memories. *Sci. Rep.* **4**, 6784 (2014).
17. Zhang, X., Ezawa, M. & Zhou, Y. Magnetic skyrmion logic gates: conversion, duplication and merging of skyrmions. *Sci. Rep.* **5**, 9400 (2015).
18. Luo, S. et al. Reconfigurable Skyrmion Logic Gates. *Nano Lett.* **18**, 1180–1184 (2018).
19. Janson, O. et al. The quantum nature of skyrmions and half-skyrmions in Cu2OSeO3. *Nat. Commun.* **5**, 5376 (2014).
20. Psaroudaki, C. & Panagopoulos, C. Skyrmion Qubits: A New Class of Quantum Logic Elements Based on Nanoscale Magnetization. *Phys. Rev. Lett.* **127**, 067201 (2021).
21. Xia, J., Zhang, X., Liu, X., Zhou, Y. & Ezawa, M. Universal Quantum Computation Based on Nanoscale Skyrmion Helicity Qubits in Frustrated Magnets. *Phys. Rev. Lett.* **130**, 106701 (2023).
22. Jiang, W. J. et al. Blowing magnetic skyrmion bubbles. *Science* **349**, 283–286 (2015).
23. Woo, S. et al. Observation of room-temperature magnetic skyrmions and their current-driven dynamics in ultrathin metallic ferromagnets. *Nat. Mater.* **15**, 501–506 (2016).
24. Soumyanarayanan, A. et al. Tunable room-temperature magnetic skyrmions in Ir/Fe/Co/Pt multilayers. *Nat. Mater.* **16**, 898–904 (2017).
25. Butykai, Á. et al. Squeezing the periodicity of Néel-type magnetic modulations by enhanced Dzyaloshinskii-Moriya interaction of 4d electrons. *npj Quantum Mater.* **7**, 26 (2022).
26. Mohanta, N. & Dagotto, E. Interfacial phase frustration stabilizes unconventional skyrmion crystals. *npj Quantum Mater.* **7**, 76 (2022).
27. Jonietz, F. et al. Spin Transfer Torques in MnSi at Ultralow Current Densities. *Science* **330**, 1648–1651 (2010).
28. Tomasello, R. et al. Electrical detection of single magnetic skyrmion at room temperature. *AIP Adv.* **7**, 056022 (2017).
29. Iwasaki, J., Mochizuki, M. & Nagaosa, N. Current-induced skyrmion dynamics in constricted geometries. *Nat. Nanotechnol.* **8**, 742–747 (2013).
30. Moreau-Luchaire, C. et al. Additive interfacial chiral interaction in multilayers for stabilization of small individual skyrmions at room temperature. *Nat. Nanotechnol.* **11**, 444–448 (2016).
31. Legrand, W. et al. Room-Temperature Current-Induced Generation and Motion of sub-100 nm Skyrmions. *Nano Lett.* **17**, 2703–2712 (2017).
32. Kern, L.-M. et al. Deterministic Generation and Guided Motion of Magnetic Skyrmions by Focused He+-Ion Irradiation. *Nano Lett.* **22**, 4028–4035 (2022).
33. Zeissler, K. et al. Discrete Hall resistivity contribution from Neel skyrmions in multilayer nanodiscs. *Nat. Nanotechnol.* **13**, 1161–1166 (2018).
34. Maccariello, D. et al. Electrical detection of single magnetic skyrmions in metallic multilayers at room temperature. *Nat. Nanotechnol.* **13**, 233–237 (2018).

35. Julliere, M. Tunneling between ferromagnetic films. *Phys. Lett. A* **54**, 225–226 (1975).
36. Parkin, S. S. et al. Giant tunnelling magnetoresistance at room temperature with MgO (100) tunnel barriers. *Nat. Mater.* **3**, 862–867 (2004).
37. Ikeda, S. et al. A perpendicular-anisotropy CoFeB-MgO magnetic tunnel junction. *Nat. Mater.* **9**, 721–724 (2010).
38. Kasai, S., Sugimoto, S., Nakatani, Y., Ishikawa, R. & Takahashi, Y. K. Voltage-controlled magnetic skyrmions in magnetic tunnel junctions. *Appl. Phys. Expr.* **12**, 083001 (2019).
39. Penthorn, N. E., Hao, X., Wang, Z., Huai, Y. & Jiang, H. W. Experimental Observation of Single Skyrmion Signatures in a Magnetic Tunnel Junction. *Phys. Rev. Lett.* **122**, 257201 (2019).
40. Alamdar, M. et al. Domain wall-magnetic tunnel junction spin–orbit torque devices and circuits for in-memory computing. *Appl. Phys. Lett.* **118**, 112401 (2021).
41. Li, S. et al. Experimental demonstration of skyrmionic magnetic tunnel junction at room temperature. *Sci. Bull.* **67**, 691–699 (2022).
42. Guang, Y. et al. Electrical Detection of Magnetic Skyrmions in a Magnetic Tunnel Junction. *Adv. Electron. Mater.* **9**, 2200570 (2023).
43. Chen, S. et al. All-electrical skyrmionic magnetic tunnel junction. *Nature* **627**, 522–527 (2024).
44. Urrestarazu Larrañaga, J. et al. Electrical Detection and Nucleation of a Magnetic Skyrmion in a Magnetic Tunnel Junction Observed via Operando Magnetic Microscopy. *Nano Lett.* **24**, 3557–3565 (2024).
45. Raab, K. et al. Brownian reservoir computing realized using geometrically confined skyrmion dynamics. *Nat. Commun.* **13**, 6982 (2022).
46. Zhang, S., Zhang, J., Wen, Y., Chudnovsky, E. M. & Zhang, X. Creation of a thermally assisted skyrmion lattice in Pt/Co/Ta multilayer films. *Appl. Phys. Lett.* **113**, 192403 (2018).
47. Raymenants, E. et al. Nanoscale domain wall devices with magnetic tunnel junction read and write. *Nat. Electron.* **4**, 392–398 (2021).
48. Yu, G. et al. Room-Temperature Skyrmion Shift Device for Memory Application. *Nano Lett.* **17**, 261–268 (2017).
49. Hayakawa, J., Ikeda, S., Lee, Y. M., Matsukura, F. & Ohno, H. Effect of high annealing temperature on giant tunnel magnetoresistance ratio of CoFeB/MgO/CoFeB magnetic tunnel junctions. *Appl. Phys. Lett.* **89**, 232510 (2006).
50. Lim, S. T., Tran, M., Chenchen, J. W., Ying, J. F. & Han, G. Effect of different seed layers with varying Co and Pt thicknesses on the magnetic properties of Co/Pt multilayers. *J. Appl. Phys.* **117**, 17A731 (2015).
51. Pollard, S. D. et al. Observation of stable Néel skyrmions in cobalt/palladium multilayers with Lorentz transmission electron microscopy. *Nat. Commun.* **8**, 14761 (2017).
52. McVitie, S. et al. A transmission electron microscope study of Néel skyrmion magnetic textures in multilayer thin film systems with large interfacial chiral interaction. *Sci. Rep.* **8**, 5703 (2018).
53. Hrabec, A. et al. Current-induced skyrmion generation and dynamics in symmetric bilayers. *Nat. Commun.* **8**, 15765 (2017).
54. Koshibae, W. et al. Memory functions of magnetic skyrmions. *Jpn. J. Appl. Phys.* **54**, 053001 (2015).
55. Chen, H., Bouckaert, W. & Majetich, S. A. Tunnel magnetoresistance detection of skyrmions. *J. Magn. Magn. Mater.* **541**, 168552 (2022).
56. Vansteenkiste, A. et al. The design and verification of MuMax3. *AIP Adv.* **4**, 107133 (2014).

Acknowledgements

The work carried out at Tsinghua University is supported by the National Natural Science Foundation of China (NSFC) under the distinguished Young Scholar program (Grant No. 12225409), the Basic Science Center Project (Grant No. 52388201), the general program (Grant Nos. 52271181), the National Key R&D Program of China (Grant No. 2022YFA1405100), and the Innovation Program for Quantum Science and Technology (Grant No. 2023ZD0300500). The work carried out at King Abdullah University of Science and Technology (KAUST) is supported by KAUST Office of Sponsored Research (OSR) under Award Nos. ORA-CRG8-2019-4081 and ORA-CRG10-2021-4665. The work carried out at Nanjing University is supported by NFSC (62274086). J.L. acknowledge the support from the Basic Science Center Project of NFSC (Grant Nos. 12304160) and the Research Foundation from NUDT (Grant No.23-ZZCX-ZZGC-01-02). Y.Z. acknowledges support from the Shenzhen Peacock Group Plan (KQTD20180413181702403), the Guangdong Special Support Project (2019BT02X030), the Shenzhen Fundamental Research Fund (Grant No. JCYJ20210324120213037), the Guangdong Basic and Applied Basic Research Foundation (2021B1515120047), the National Natural Science Foundation of China (12374123), and the 2023 SZSTI stable support scheme. We would like to thank Dr. Y.C. Guan for helping with the electrical measurements and for providing helpful discussion.

Author contributions

W.J. conceived and designed the experiments. A.C. and M.Z. fabricated the MTJ film. A.C., B.F., L.Z., D.Z., M.Z. S.W., E.L. and S.H. performed lithographic processing. C.L. conducted the LTEM measurement. P.Y.H., W.C.Y and M.Z. performed the MFM experiments. M.Z., A.C., L.W. H.B. and L.Z. did the electrical characterizations. J.L, M.Z., L.S., K.S. and Y.Z. carried out the micromagnetic simulation and analyzed the data. M.Z. wrote the manuscript with the help of W.J. All authors commented on the manuscript. M.Z., A.C., P.Y.H., C.L., and L.S. contributed equally to this work.

Competing interests

The authors declare no competing interests.

Additional information

Supplementary information The online version contains supplementary material available at https://doi.org/10.1038/s41535-024-00655-1.

Correspondence and requests for materials should be addressed to Jiahao Liu, Yong-Lei Wang, Xixiang Zhang or Wanjun Jiang.